

# **MoS<sub>2</sub>-based optical bistability in silver-Bragg reflector multilayer structure at visible light band**

Songqing Tang<sup>1</sup>, Mengjiao Ren<sup>1</sup>, Zhiheng Li<sup>1</sup>, Zhiwei Zheng<sup>1</sup>, Leyong Jiang<sup>1,2,\*</sup>  
<sup>1</sup>*School of Physics and Electronics, Hunan Normal University, Changsha 410081, China*

<sup>2</sup>*Post Moore era laboratory, Hunan Normal University, Changsha 410081, China*

Corresponding Author: \*jiangly28@hunnu.edu.cn

## **Abstract**

In this paper, we present a theoretical analysis of the optical bistability in a metallic silver-Bragg reflector structure by embedding bilayer MoS<sub>2</sub> at the visible band. The nonlinear OB is achieved due to the nonlinear conductivity of the bilayer MoS<sub>2</sub> and the excitation of the optical Tamm state at the interface between the silver and the Bragg reflector. It is found that the hysteresis behaviour and the threshold width of the OB can be effectively tuned by varying the incident light wavelength. In addition, the optical bistable behaviour of the structure can be adjusted by varying the position of the MoS<sub>2</sub> inset in the defect layer, incident angle and the structural parameters of the spacer layer. Although the current threshold cannot be commercialized, we believe that this solution will provide a meaningful path reference for low threshold bistability in the visible light band.

**Keywords:** optical bistability; nonlinear MoS<sub>2</sub>; optical Tamm state; visible light band.

## 1. Introduction

Optical bistability (OB) is a nonlinear optical phenomenon in which two different stable output states are produced for a given input state in an optical system [1]. The characteristic curve of OB shows a distinct hysteresis loop relationship with delay and abrupt change, and therefore it is widely used in all-optical switches [2,3], all-optical logic gates [4,5], biosensors [6], optical storage [7], computing [8], etc. Due to the large size and small material nonlinear coefficient in the design of conventional optical bistable devices, which requires a high incident power to achieve significant OB phenomena, which can cause damage to the optics and also fail to meet the requirements of small size and low power consumption in integrated optics. In recent years, micro and nano technologies have become increasingly mature and developed rapidly, people start to seek OB phenomena in micro and nano structures, based on photonic crystals[9,10],Fabry-Perot cavity [11,12],hyper-bolic metamaterials [13], and nonlinear ring resonator structures [14], and a series of OB phenomena in micro and nano structures have been proposed one after another. We know that there is a positive correlation between the threshold of OB and the nonlinear coefficient of the material, and the higher the nonlinear coefficient of the material the lower the threshold in achieving OB. In recent years, The two-dimensional materials graphene and three-dimensional Dirac semimetals stand out among the many materials due to their large nonlinear coefficients in the terahertz band [15,16], and OB studies based on graphene and Dirac semimetals have been successively proposed. For example, OB in graphene-on-Kerr nonliner surface [17], OB in graphene-Bragg

reflectorstructure[18], OB in one-dimensional photonic crystal heterostructures based on Dirac semimetals [19] have been reported. Although OB phenomena based on graphene and Dirac semimetals have been studied extensively, the research has been mostly limited to the terahertz band. At present, OB research in the visible band is still in infancy. Therefore, the search for new ways to tune OB in the visible band is being tried by researchers.

Recently, it has been found that the bilayer MoS<sub>2</sub> has a high third-order nonlinear coefficient in the visible band, which has attracted attention. The monolayer MoS<sub>2</sub> molecule has a linear electro-optical effect (Pockels effect) [20,21] and the bilayer MoS<sub>2</sub> molecule has a secondary electro-optical effect (Kerr effect) [20]. The bilayer MoS<sub>2</sub> molecular gives a large nonlinear coefficient in the visible band based on the Kerr effect[22], which provides nonlinear conditions to achieve OB. Also,we know that the wave vector in vacuum can be tuned by changing the wavelength of the incident light, thereby changing the third-order nonlinear conductivity of MoS<sub>2</sub>, which provides the possibility for the implementation of tunable OB. Compared to terahertz band based graphene and 3D Dirac semimetallic OB studies, this study provides a way to tune OB in the visible band based on MoS<sub>2</sub>, which makes this work meaningful. Optical Tamm state (OTS) are lossless interface modes localised at two interfaces with different media [23]. They have strong localization, be easily excited, surface-constrained properties[24]. Current studies on OTS are mainly based on metal-Bragg reflector structure[25,26] and one-dimensional photonic crystal heterostructure [27,28]. We know that local field enhancement contributes positively

to the threshold reduction of OB, which is beneficial for achieving OB[29].

In this paper, we theoretically analysis the OB phenomenon in a silver-Bragg reflector structure based on nonlinear MoS<sub>2</sub>. The results show that OTS is generated at the interface between the Bragg reflector and the defective layer, which leads to an enhancement of the local field. Furthermore, inserting a bilayer of MoS<sub>2</sub> molecular into the multilayer structure provides a nonlinear condition for the generation of OB. At the same time, we can dynamically tune the hysteresis behaviour and threshold width of the OB by varying the wavelength of the incident light. This OB study has the properties of simple structure, easy preparation and OB realisation in the visible band band, for which we believe that this study can provide a new idea for the regulation of OB in optical fields such as all-optical switches and all-optical logic gates in the future.

## 2. Theoretical Model and Method

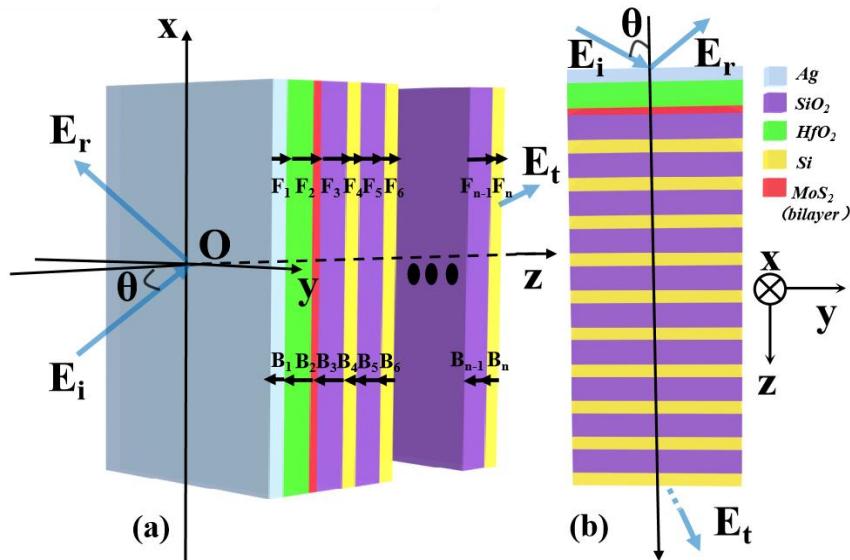


**Fig. 1.** Schematic diagram of a silver-Bragg reflector structure by embedding bilayer MoS<sub>2</sub>. (a) three-dimensional view (b) two-dimensional view. where the incident angle between the incident

light and the z-axis is  $\theta$ . The bilayer of MoS<sub>2</sub> molecular is between the spacer layer HfO<sub>2</sub> and the Bragg reflector,  $E_i$  is the incident electric field,  $E_r$  is the reflected electric field,  $E_t$  is the transmitted electric field.  $F_m$  and  $B_m$  represent the forward and reverse electric field in the medium ( $m=1,2,3,4,\dots,22$ ).

We consider a one-dimensional multilayer structure with a silver-Bragg reflector and a bilayer MoS<sub>2</sub>. As shown in Fig. 1, Fig. 1(a) shows the three-dimensional view and Fig. 1(b) shows the two-dimensional view. In this structure, the Bragg reflector consists of alternating periodic arrangements of dielectric A (SiO<sub>2</sub>) and dielectric B (Si), period is set to  $T=10$ . The refractive index of medium A is  $n_A = 1.46$ , and that of medium B is  $n_B = 2.82$ . In this Bragg reflector, the central wavelength is set to  $\lambda_c = 660$  nm, the thickness of medium A is  $d_A = \lambda_c / 4n_A$ , and the thickness of medium B is  $d_B = \lambda_c / 4n_B$ . The bilayer of MoS<sub>2</sub> molecular is embedded between the spacer layer and the Bragg reflector. The silver placed at the top of the structure and the relative permittivity of silver can be expressed as [30]:

$$\varepsilon_{Ag}(\omega) = \varepsilon_{\infty} - \omega_p^2 / (\omega^2 + i\tau\omega), n_{Ag}(\omega) = \varepsilon_{\infty} - \omega_p^2 / (\omega^2 + i\tau\omega), \quad (1)$$

where  $\varepsilon_{\infty} = 5$ ,  $\hbar\omega_p = 9$  eV,  $\hbar\tau = 18$  eV. In this study, we set the thickness of silver to  $d_{Ag} = 30$  nm. The refractive index of the spacer layer HfO<sub>2</sub> is set to  $n_s = 1.95$  and the thickness is designed to be  $d_s = 70$  nm. Each monolayer MoS<sub>2</sub> has a thickness of  $A = 0.65$  nm.

Based on the current mature micro and nano fabrication technology, structures with the above structural parameters can be easily manufactured. Meanwhile, the bilayer MoS<sub>2</sub> molecular has a strong kerr effect in the visible band. Here, we describe

MoS<sub>2</sub> using third-order nonlinear polarizability, third-order nonlinear conductivity, and linear conductivity. Neglecting the effect of external magnetic fields under random phase conditions, the linear dielectric constant of MoS<sub>2</sub> molecule can be expressed as [31]:

$$\varepsilon_{(\omega)}^{(1)} = \varepsilon_{\infty 2} + \sum_{i=0}^5 \frac{a_i \omega_p^2}{\omega_i^2 - \omega^2 - i b_i \omega} - \frac{2\alpha}{\sqrt{\pi}} \text{Dawson}F\left(\frac{\mu - \hbar\omega}{\sqrt{2}\sigma}\right) + \alpha \exp\left(\frac{-(\hbar\omega - \mu)^2}{2\sigma^2}\right), \quad (2)$$

where  $\alpha = 23.234$ ,  $\mu = 2.7723$  eV, and  $\sigma = 0.3089$  eV.  $\varepsilon_{\infty 2} = 4.44$ , which is the DC electrical permittivity.  $a_i$  is the oscillator strength,  $b_i$  is the damping coefficient,  $\omega_i$  is the response frequency and  $\omega_p = 7 \times 10^{12}$  rad/s is the plasma frequency[32]. The first order linear conductivity ( $\sigma_{(\omega)}^{(1)}$ ) of MoS<sub>2</sub>:

$$\sigma_{(\omega)}^{(1)} = \frac{\Lambda k_0}{i \eta_0} (\varepsilon_{(\omega)}^{(1)} - 1), \quad (3)$$

Where  $\eta_0 = 377 \Omega$  is the vacuue resistivity, and  $k_0 = \omega/c$  is the wave vector in vacuue. The third order nonlinear conductivity( $\varepsilon_{(\omega)}^{(3)}$ ) of MoS<sub>2</sub>:

$$\sigma_{(\omega)}^{(3)} = \frac{2\Lambda k_0}{i \eta_0} \frac{3m_e \omega_0^2 \varepsilon^3}{d^2 N^3 e^4} [(\varepsilon_{(\omega)}^{(1)} - 1)^3] (\varepsilon_{(-\omega)}^{(1)} - 1), \quad (4)$$

where  $d = 3\text{\AA}$ ,  $N = 10^{28} \text{ m}^{-3}$  is the atomic number desity[22]. The total conductivity of MoS<sub>2</sub> can be expressed as:

$$\sigma_{(\omega)} = \sigma_{(\omega)}^{(1)} + \sigma_{(\omega)}^{(3)} \left| E_{2y}(z = d_{\text{Ag}} + d_s) \right|^2, \quad (5)$$

the equations of  $\sigma_{(\omega)}^{(1)}$ ,  $\sigma_{(\omega)}^{(3)}$  and  $\sigma_{(\omega)}$  show that the electrical conductivity of MoS<sub>2</sub> has an important relationship with the wave vector in vacuum. We assume that the electromagnetic wave propagates along the z-axis, the surface on which the silver is located is  $z = 0$ , and the MoS<sub>2</sub> is parallel to the plane of the x-axis and y-axis.

Considering only TE polarisation, the electromagnetic field incident on the surface of the silver layer from the air according to Maxwell equation can be expressed as:

$$\begin{cases} E_{iy} = E_i e^{ik_{iz}z} e^{ik_x x} + E_r e^{-ik_{iz}z} e^{ik_x x}, \\ H_{ix} = -\frac{k_{iz}}{\mu_0 \omega} E_i e^{ik_{iz}z} e^{ik_x x} + \frac{k_{iz}}{\mu_0 \omega} E_r e^{-ik_{iz}z} e^{ik_x x}, \\ H_{iz} = \frac{k_x}{\mu_0 \omega} E_i e^{ik_{iz}z} e^{ik_x x} + \frac{k_x}{\mu_0 \omega} E_r e^{-ik_{iz}z} e^{ik_x x}, \end{cases} \quad (6)$$

where  $k_{0z} = k_0 \cos(\theta)$ ,  $k_{0x} = k_0 \sin(\theta)$ ,  $u_0$  denote vacuum permeability,  $E_i$  denotes incident electric field,  $E_r$  denotes reflected electric field and  $E_t$  denotes the transmitted electric field.  $F_m$  denotes the forward electric field and  $B_m$  denotes the reverse electric field in the m-layer of the dielectric.

Similarly, the electric and magnetic fields in the silver layer can be expressed as:

$$\begin{cases} E_{1y} = F_1 e^{ik_{1z}z} e^{ik_x x} + B_1 e^{-ik_{1z}z} e^{ik_x x}, \\ H_{1x} = -\frac{k_{1z}}{u_0 \omega} F_1 e^{ik_{1z}z} e^{ik_x x} + \frac{k_{1z}}{u_0 \omega} B_1 e^{-ik_{1z}z} e^{ik_x x}, \\ H_{1z} = \frac{k_x}{u_0 \omega} F_1 e^{ik_{1z}z} e^{ik_x x} + \frac{k_x}{u_0 \omega} B_1 e^{-ik_{1z}z} e^{ik_x x}, \end{cases} \quad (7)$$

The electric and magnetic fields in the HfO<sub>2</sub> layer can be represented as:

$$\begin{cases} E_{2y} = F_2 e^{ik_{2z}(z-d_{Ag})} e^{ik_x x} + B_2 e^{-ik_{2z}(z-d_{Ag})} e^{ik_x x}, \\ H_{2x} = -\frac{k_{2z}}{u_0 \omega} F_2 e^{ik_{2z}(z-d_{Ag})} e^{ik_x x} + \frac{k_{2z}}{u_0 \omega} B_2 e^{-ik_{2z}(z-d_{Ag})} e^{ik_x x}, \\ H_{2z} = \frac{k_x}{u_0 \omega} F_2 e^{ik_{2z}(z-d_{Ag})} e^{ik_x x} + \frac{k_x}{u_0 \omega} B_2 e^{-ik_{2z}(z-d_{Ag})} e^{ik_x x}, \end{cases} \quad (8)$$

For a medium m ( $m = 3,4,5,6... .22$ ), the electric and magnetic fields can be expressed as:

$$\begin{cases} E_{my} = F_m e^{ik_{jz}[z-(d_{Ag}+d_s+\alpha d_A+\beta d_B)]} e^{ik_x x} + B_m e^{-ik_{jz}[z-(d_{Ag}+d_s+\alpha d_A+\beta d_B)]} e^{ik_x x}, \\ H_{mx} = -\frac{k_{jz}}{u_0 \omega} F_m e^{ik_{jz}[z-(d_{Ag}+d_s+\alpha d_A+\beta d_B)]} e^{ik_x x} + \frac{k_{jz}}{u_0 \omega} B_m e^{-ik_{jz}[z-(d_{Ag}+d_s+\alpha d_A+\beta d_B)]} e^{ik_x x}, \\ H_{mz} = \frac{k_x}{u_0 \omega} F_m e^{ik_{jz}[z-(d_{Ag}+d_s+\alpha d_A+\beta d_B)]} e^{ik_x x} + \frac{k_x}{u_0 \omega} B_m e^{-ik_{jz}[z-(d_{Ag}+d_s+\alpha d_A+\beta d_B)]} e^{ik_x x}, \end{cases} \quad (9)$$

In the above equation. If  $m$  is an odd number,  $j = a$ ,  $\alpha = (m-1)/2$ ,  $\beta = (m-3)/2$ . If  $m$  is an even number,  $j = b$ ,  $\alpha = m/2 - 1$ ,  $\beta = m/2 - 1$ ,  $k_{jz} = \sqrt{k_0^2 n_j^2 - k_x^2}$ ,  $j = \{s, a, b\}$ .

Finally, the electric and magnetic fields in the substrate media can be expressed

as:

$$\begin{cases} E_{(n+1)y} = E_t e^{ik_{oz}[z-(d_{Ag}+d_s+10d_A+10d_B)]} e^{ik_x x}, \\ H_{(n+1)x} = -\frac{k_{oz}}{u_0 \omega} E_t e^{ik_{oz}[z-(d_{Ag}+d_s+10d_A+10d_B)]} e^{ik_x x}, \\ H_{(n+1)z} = \frac{k_x}{u_0 \omega} E_t e^{ik_{oz}[z-(d_{Ag}+d_s+10d_A+10d_B)]} e^{ik_x x}, \end{cases} \quad (10)$$

According to the boundary conditions at  $z = 0$ , the electric field and the magnetic field are continuous, there are  $E_{iy}(z=0) = E_{1y}(z=0)$  and  $H_{ix}(z=0) = H_{1x}(z=0)$ .

At  $z = d_{Ag}$ , there are  $E_{1y}(z=0) = E_{2y}(z=0)$ ,  $H_{1x}(z=0) = H_{2x}(z=0)$ . At  $z = d_{Ag} + d_s$ , the electric field is continuous and the magnetic field is discontinuous, there are

$$H_{2x}(z = d_A + d_s) - H_{3x}(z = d_A + d_s) = \sigma E_{2y}(z = d_A + d_s), \quad E_{2y}(z = d_A + d_s) = E_{3y}(z = d_A + d_s).$$

At  $z = d_{Ag} + d_s + \alpha d_A + \beta d_B$ , the electric field is continuous and the condition is satisfied

$$E_{my}(z = d_{Ag} + d_s + \alpha d_A + \beta d_B) = E_{(m+1)y}(z = d_{Ag} + d_s + \alpha d_A + \beta d_B), \text{ and the magnetic field is continuous } H_{mx}(z = d_{Ag} + d_s + \alpha d_A + \beta d_B) = H_{(m+1)x}(z = d_{Ag} + d_s + \alpha d_A + \beta d_B).$$

where  $m=1,2,3,4,\dots,22$ . After the all, the electric field versus incident electric field and the reflectance versus incident electric field curves for the whole structure can

be obtained in directly by substituting equation (6)(7)(8)(9)(10) into the above boundary conditions.

### 3. Results and Discussions

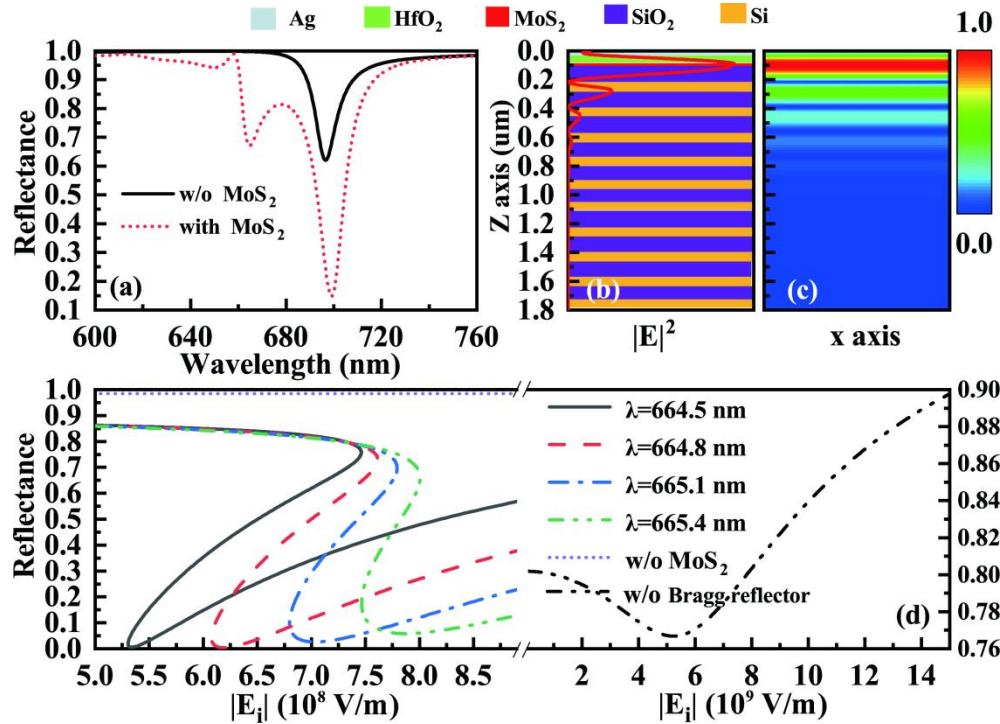


**Fig. 2.** (a) Reflectance versus incident wavelength for  $\theta = 0^\circ$ . (b) One-dimensional line plot (c) Multi-colour plot distribution of the field enhancement of the silver-Bragg reflector structure (with the bilayer of MoS<sub>2</sub> sandwiched in between). (d) Reflectance versus incident electric field with and without MoS<sub>2</sub> and with and without spacer layer HfO<sub>2</sub> for different incident wavelengths .

In the section, we first discuss the variation of reflectance with incident light wavelength using the transmission matrix method. Fig. 2(a) shows the plot when the incident light is incident vertically ( $\theta=0^\circ$ ) on the microcavity structure. Both the black solid line and the red dashed line in the figure show the reflectance versus incident light wavelength curve. The black solid line shows the reflectance versus incident wavelength without the addition of MoS<sub>2</sub> in the microcavity structure. As can be seen from the graph, the black curve at  $\lambda=696.7$  nm shows a significant

decrease in the reflectance peak. It is known that the OTS need to satisfy  $r_{\text{Ag}}r_{\text{DBR}}\exp(2i\phi) \approx 1$  when excited [33], where  $r_{\text{Ag}}$  and  $r_{\text{DBR}}$  represent the reflectance of the electromagnetic wave at the silver interface and the surface of the Bragg reflector, respectively.  $\phi$  is the phase change of the electromagnetic wave as it propagates through the top layer. After simplifying the equations, the OTS excitation conditions can be expressed as  $|r_{\text{Ag}}||r_{\text{DBR}}| \approx 1$ ,  $\text{Arg}(r_{\text{Ag}}r_{\text{DBR}}\exp(2i\phi)) \approx 0$ . Keeping the original structural parameters in Fig. 1 unchanged, the reflectance of the silver surface and the Bragg reflector surface were calculated, there are  $r_{\text{Ag}} = -0.5604 - 0.7506i$  and  $r_{\text{DBR}} = 0.8677 - 0.4970i$ , which can be seen that the black solid line reflection anomaly in Fig. 2(a) is due to the excitation of the OTS. The red dashed line in Fig. 2(b) shows the reflectance versus incident light wavelength with the addition of MoS<sub>2</sub> in the structure. It is easy to see that there is a significant deepening of the decrease and the minimum value of reflectance nearly 0.1. To better show the Tamm plasmon in the silver-Bragg reflector structure. We are set to the incident light wavelength  $\lambda = 696.7$  nm. In Fig. 2(b) and Fig. 2(c), the normalised field distribution graph for the whole structure were plotted based on the original structure parameters in Fig. 1, and the used simulation software is COMSOL. In Fig. 2(b) we have divided the entire structure zones according to the proportion of the thickness of the material. In combination with the multi-colour Fig. 2(c), it is found that the electric field shows a clear field enhancement effect at the interface between the defect layer and the Bragg reflector.

By using the calculation method in the second part ,we obtain the relationship between the incident electric field and reflected electric field in Fig. 2(d) with the plotting software ORIGIN. In order to obtain a suitable reflectance, the incident light wavelength was set to 664.5 nm, and the other structural parameters were kept the same as the original parameters in Fig.1 during the calculation. The resulting curve is the solid black line in Fig. 2(d), and shows a hysteresis line relationship. With the MoS<sub>2</sub> Removed, the reflectance of the structure is approximately 1. As the incident electric field changes, the reflectance is almost unchanged, and there is no hysteresis line relationship between the reflectance and the incident electric field  $E_i$ . This is because the bilayer MoS<sub>2</sub> molecular has a high third-order nonlinear conductivity in the visible band. However, under nonlinear conditions provided by the MoS<sub>2</sub>, the reflectance and the incident electric field  $E_i$  exhibit a hysteresis relationship. With the Bragg reflector removed, the OB precursor between the reflectance and the incident electric field is starting to emerge, but it corresponds to the incident electric field of about  $10^9$  V/m. Comparing the incident electric field  $10^8$  V/m with the Bragg reflector, it is clear that the excitation of OTS has a very positive effect on the reduction of the OB threshold.

From equation (3)(4) we know that changing the wavelength of the incident light can change the wave vector in the vacuum  $k_0$ , which can indirectly change the first order linear conductivity ( $\sigma_{(\omega)}^{(1)}$ ) and the third order nonlinear conductivity ( $\sigma_{(\omega)}^{(3)}$ )

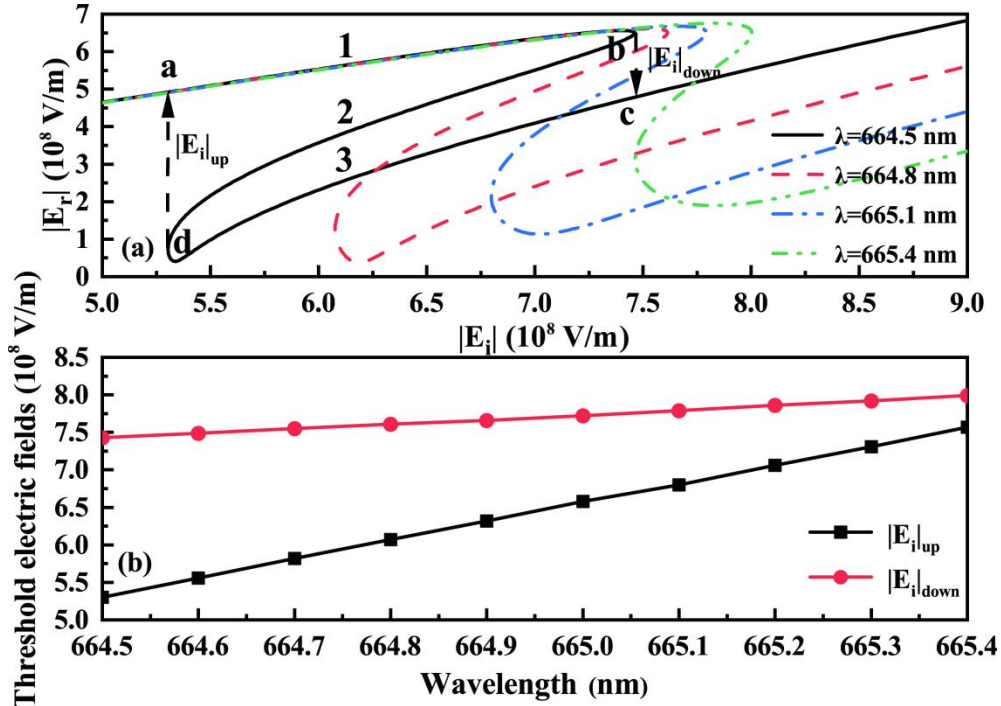


**Fig.3.** (a) Reflected electric field  $E_r$  versus incident electric field  $E_i$  for different incident light wavelengths. (b) The upper and lower thresholds of the incident electric field  $E_i$  versus the incident wavelength.

of MoS<sub>2</sub>. It can be clearly found that changing the wavelength of the incident light can obviously change the total conductivity of the MoS<sub>2</sub> from equation (5). Based on the above theoretical analysis, we can use the incident light wavelength as an tool to regulate this OB.

Next, we explore the effect of varying the wavelength of the incident light on the OB. Keeping the structural parameters of Fig. 1 constant and varying only the incident light wavelength, the reflected electric field was simulated numerically with the variation of the incident electric field. By calculation, we obtain the relationship between the reflected electric field  $E_r$  and the incident electric field  $E_i$ , as shown in Fig. 3(a). For example, taking the OB curve at the incident light wavelength of  $\lambda=664.5$  nm, connecting the markers gives the S-curve a-1-b-2-d-3-c.

when  $E_i$  is small,  $E_r$  increases with  $E_i$  increases, which corresponds to the a-1-b process, which is a steady state. As incident electric field  $E_i$  continues to increase until  $|E_i|_{\text{down}} = 7.43 \times 10^8 \text{ V/m}$ ,  $E_r$  jumps to another stable state, corresponding to the c-3-d process. At this point, even if  $E_i$  continues to decrease,  $E_r$  does not immediately return to the stable state of a-1-b. Conversely, when  $E_i$  is large, the system is in the second steady state,  $E_r$  decreases as  $E_i$  decreases, and when  $E_i$  decreases to  $|E_i|_{\text{up}} = 5.30 \times 10^8 \text{ V/m}$ ,  $E_r$  jumps from the second steady state c-3-d to the first steady state a-1-b. The b-2-d process is unstable, and  $E_r$  increases as  $E_i$  increases, but the increase is unstable and the curve is not observed in the experiment. Thus, this creates two jump points b and d and a bistable loop. The OB of this multilayer structure operates in the a-b interval and the c-d interval, where one  $E_i$  corresponds to two  $E_r$ . This leads to a hysteresis width  $\Delta |E_i| = |E_i|_{\text{down}} - |E_i|_{\text{up}} = 2.13 \times 10^8 \text{ V/m}$ . Clearly, this is the OB phenomenon we are looking for, in which the nonlinear properties of MoS<sub>2</sub> play a decisive role in obtaining this OB. Furthermore, the controlled conductivity of MoS<sub>2</sub> in the visible band offers the nonlinear condition to achieve a tunable OB.

In order to describe the relationship between  $E_r$  and  $E_i$  more intuitively, the curve of the hysteresis width with the incident light wavelength is plotted, as shown in Figure 3(b). As can be seen from the figure, different values of the incident light wavelength not only affect the upper and lower thresholds of OB, but also have a effect on the hysteresis width. As the incident light wavelength continues to increase, the upper threshold becomes larger and the lower threshold also becomes larger.

However, the upper threshold of the reflected electric field increases faster than the lower threshold. Therefore, the hysteresis width becomes progressively narrower as the wavelength of the incident light continues to increase. For example, when the incident wavelength is  $\lambda=664.8$  nm, the upper threshold is  $|E_i|_{\text{up}}=6.07\times 10^8$  V/m, the lower threshold is  $|E_i|_{\text{down}}=7.61\times 10^8$  V/m and the hysteresis width is  $\Delta|E_i|=1.54\times 10^8$  V/m. When the incident wavelength is  $\lambda=665.1$  nm, the upper threshold is  $|E_i|_{\text{up}}=6.80\times 10^8$  V/m, the lower threshold is  $|E_i|_{\text{down}}=7.79\times 10^8$  V/m and the hysteresis width is  $\Delta|E_i|=0.99\times 10^8$  V/m. It is easy to see that increasing the incident wavelength contributes positively to the reduction of the OB threshold. In summary, the incident light wavelength can tune the OB threshold and the hysteresis width, providing a reference method for obtaining dynamically tunable OB devices.

Next, we discuss the effect of the MoS<sub>2</sub> in the defect layer HfO<sub>2</sub> at different positions on the OB phenomenon. Keeping the total thickness of the defect layer HfO<sub>2</sub>  $d_s$  constant, the position of MoS<sub>2</sub> embedded in the defect layer HfO<sub>2</sub> is changed so that the defect layer HfO<sub>2</sub> is divided into an upper part  $d_{s1}$  and a lower part  $d_{s2}$ . The incident light wavelength is fixed at  $\lambda=664.5$  nm and the other parameters are the same as those in Fig. 2(a). From Fig. 4, it can be seen that the MoS<sub>2</sub> is embedded in the spacer layer HfO<sub>2</sub>. The effect on the OB at different

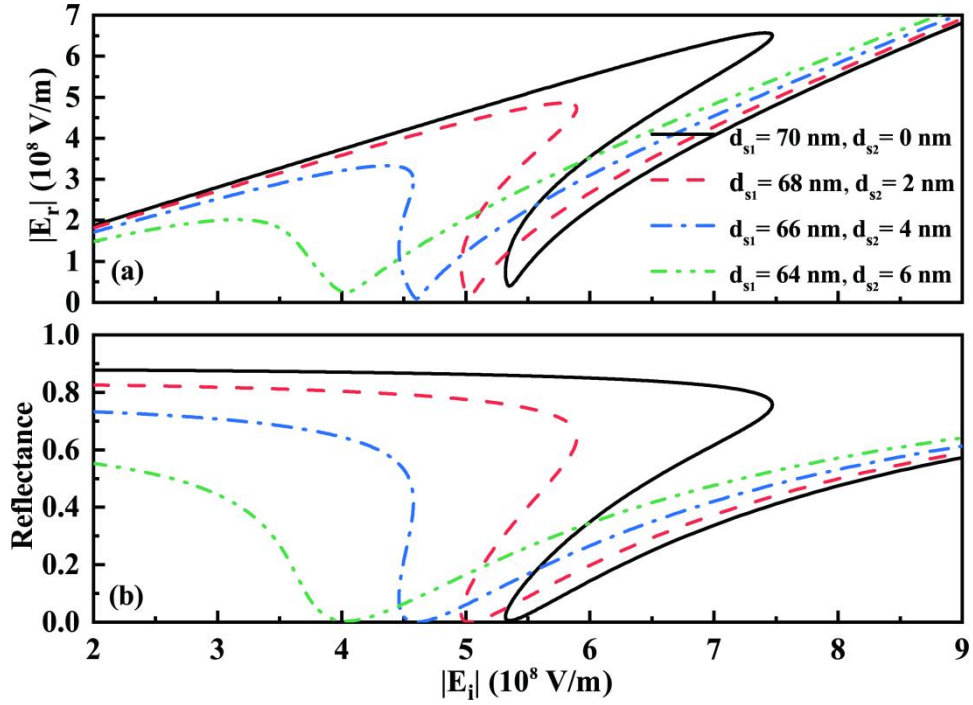


**Fig. 4.** Set the MoS<sub>2</sub> in the middle of the defect layer HfO<sub>2</sub>. Keeping the total thickness of the defect layer HfO<sub>2</sub>  $d_s$  unchanged, the position of MoS<sub>2</sub> embedded in the defect layer HfO<sub>2</sub> was changed so that the defect layer HfO<sub>2</sub> was divided into an upper part  $d_{s1}$  and a lower part  $d_{s2}$ . (a) reflected electric field and (b) reflectance versus incident electric field at an incident light wavelength of 664.5 nm.

positions is similar to the effect of changing the wavelength of the incident light on the OB, which is clearly reflected in the changes in the upper and lower threshold and the hysteresis width of the OB. The threshold magnitude and hysteresis width of the reflected electric field curve decrease as the thickness of the defect layer in the lower half  $d_{s2}$  increases, as shown in Fig. 4(a). The relationship curve between reflectance and incident electric field  $E_i$  follows a similar trend, as shown in Fig. 4(b). For example, when the thickness of the upper half of the spacer layer HfO<sub>2</sub> is  $d_{s1}=68$  nm and the thickness of the lower half is  $d_{s2}=2$  nm, the upper threshold is  $|E_i|_{up} = 4.96 \times 10^8$  V/m, the lower threshold is  $|E_i|_{down} = 5.89 \times 10^8$  V/m and the

hysteresis width is  $\Delta|E_i| = 0.93 \times 10^8$  V/m . When the spacer layer HfO<sub>2</sub> has an upper half thickness of  $d_{s1} = 66$  nm and a lower half thickness of  $d_{s2} = 4$  nm , the upper threshold is  $|E_i|_{up} = 4.44 \times 10^8$  V/m, the lower threshold is  $|E_i|_{down} = 4.57 \times 10^6$  V/m, and the hysteresis width is  $\Delta|E_i| = 0.13 \times 10^6$  V/m. We found that the OB threshold and hysteresis width slowly decrease as the thickness of the lower half of the defect layer increases after inserting MoS<sub>2</sub> into the defect layer. However, the OB threshold and hysteresis width do not decrease with the increase in the thickness of the lower half of the spacer layer, and will disappear when the thickness of the spacer layer increases to a certain value. The above results show that the OB threshold can be effectively reduced and the hysteresis width can be controllably adjusted by adjusting the position of the MoS<sub>2</sub> inserts in the defect layer, which provides another feasible method for the fabrication and design of optical bistable devices.

Immediately afterwards, we observe the effect of different angles of incidence on the OB phenomenon. The wavelength of the incident light was fixed at  $\lambda = 664.5$  nm and the other parameters were consistent with Fig. 1. From Fig. 5 we see that the bistable behaviour is sensitive to changes in the angle of incidence  $\theta$  . In Fig. 5(a), the upper threshold of the reflected electric field curve becomes smaller and smaller with increasing incident angle, and the lower threshold also becomes smaller and smaller. However, the lower limit threshold decreases faster than the upper limit threshold, which can lead to a decrease in the hysteresis width. For example, when  $\theta = 6^\circ$ , there are  $|E_i|_{up} = 5.26 \times 10^8$  V/m and  $|E_i|_{down} = 7.17 \times 10^6$  V/m, thus the hysteresis width is  $\Delta|E_i| = 1.91 \times 10^8$  V/m . When  $\theta = 12^\circ$ , the upper threshold is  $|E_i|_{up} = 5.10 \times 10^8$  V/m

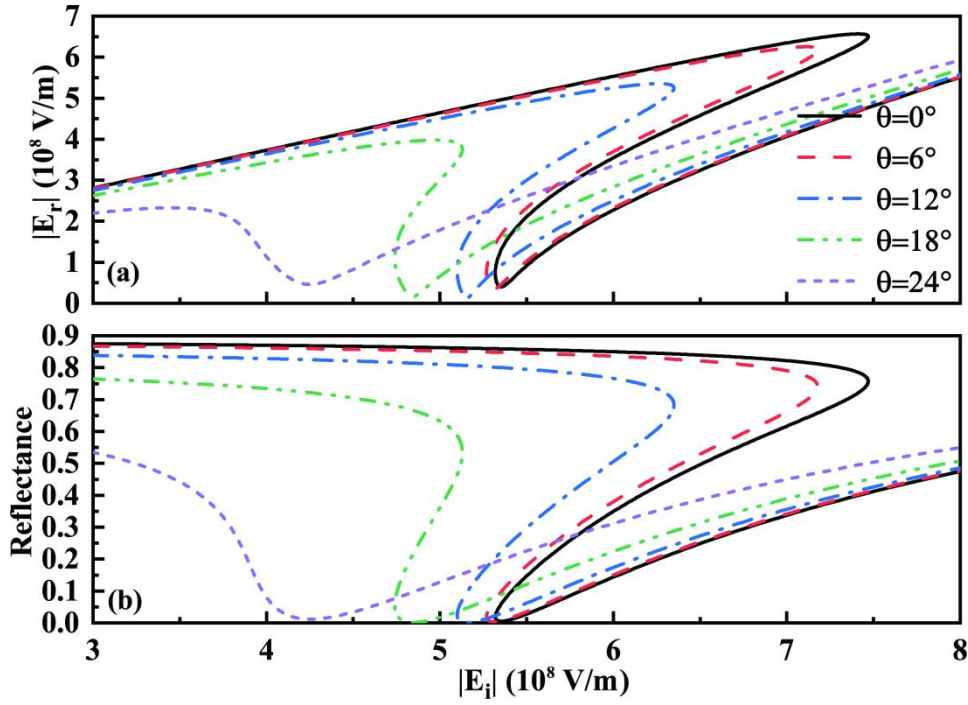
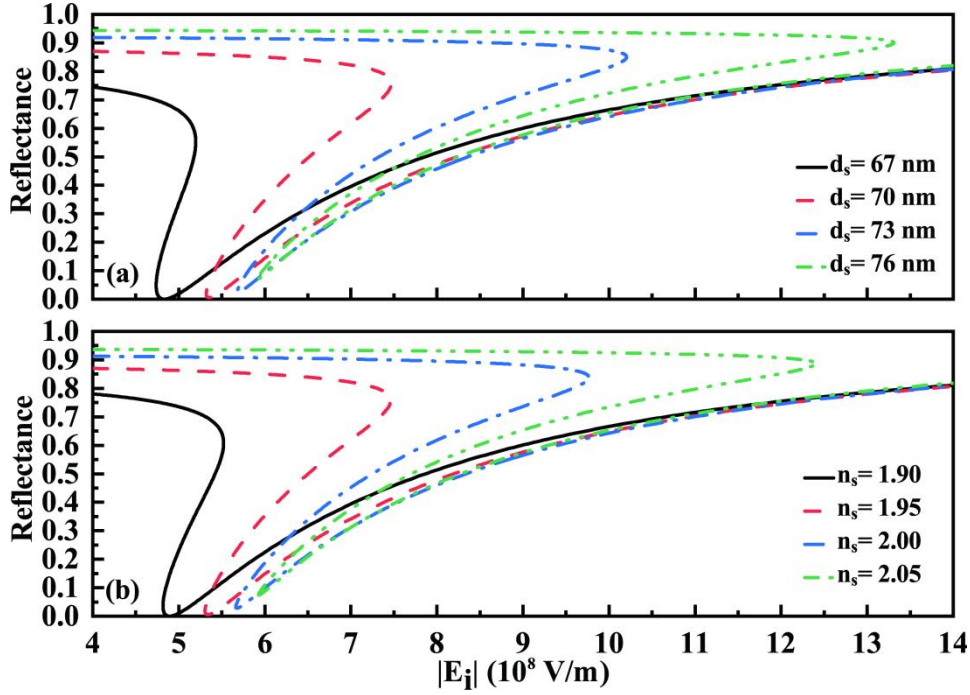


Fig.5 Relationship between (a) reflectance, (b) reflected electric field and incident electric field for different incidence angles  $\theta = 0^\circ$  ,  $\theta = 6^\circ$  ,  $\theta = 12^\circ$  ,  $\theta = 18^\circ$  ,  $\theta = 24^\circ$  .

and the lower threshold is  $|E_i|_{down} = 6.34 \times 10^8$  V/m ,  $\Delta|E_i| = 1.24 \times 10^8$  V/m . As the angle of incidence increases further to a certain angle, the hysteresis width slowly disappears. The relationship curve between the reflectance and the incident electric field follows the same trend in Fig. 5(b). The above results show that adjusting the angle of incidence can effectively reduce the threshold of OB while achieving a controlled adjustment of the hysteresis width. Therefore, a reasonable choice of the incident angle is of great practical importance for reducing the OB threshold and achieving the actual required OB hysteresis width.

Finally, we discuss the effect of the structural parameters of the defect layer on the OB phenomenon. The incident light wavelength is fixed at  $\lambda = 664.5$  nm and the other parameters remain the same as in Fig. 2(a). We plot the reflectance versus incident electric field for different defect layer thicknesses  $d_s$  and different defect layer



**Fig. 6.** (a) Reflectance versus incident electric field for spacer layers at different thicknesses 67nm, 70nm, 73nm, 76nm. (b) Reflectance versus incident electric field for different dielectric constants of 1.90, 1.95, 2.00 and 2.05.

refractive index  $n_s$ . As shown in Fig. 6(a), the upper threshold and lower threshold of OB and become larger as the defect layer thickness  $d_s$  becomes larger, but the lower threshold increases faster than the upper threshold, leading to an increase in the hysteresis width. For example, when  $d_s=73$  nm, the upper threshold is  $|E_i|_{up} = 5.68 \times 10^8$  V/m and the lower threshold is  $|E_i|_{down} = 10.18 \times 10^8$  V/m, the hysteresis width is  $\Delta|E_i| = 4.50 \times 10^8$  V/m. When  $d_s=76$  nm, the upper threshold is  $|E_i|_{up} = 5.90 \times 10^8$  V/m, the lower threshold is  $|E_i|_{down} = 13.25 \times 10^8$  V/m and the hysteresis width is  $\Delta|E_i| = 7.35 \times 10^8$  V/m. A similar pattern occurs when changing the refractive index of the defect layer, as shown in Figure 6(b). As the refractive index of the defect layer  $n_s$  becomes progressively larger, the upper threshold value of OB  $|E_i|_{up}$  and the lower threshold value  $|E_i|_{down}$  also become larger, but the lower

threshold value increases faster than the upper threshold value, resulting in an increase in the hysteresis width. Therefore, a reasonable choice of the structural parameters of the defect layer can lead to a more reasonable OB phenomenon.

#### **4. Conclusions**

In summary, we have investigated the OB phenomenon in a silver-bragg reflector structure based on a bilayer of MoS<sub>2</sub> molecular. Based on this structure a tunable OB phenomenon in the visible band range was achieved. The results show that the Tamm state based on the silver and Bragg reflector structure leads to a local electric field enhancement effect, which facilitates the realization of OB. At the same time, the large nonlinear conductivity of the bilayer of MoS<sub>2</sub> molecular provides the nonlinear conditions for the appearance of the OB phenomenon. Thereafter, after setting the initial parameters such as the incident angle, we calculated the reflected electric field and the reflectance as a function of the incident electric field. The threshold and hysteresis width of the OB were found to be modulated by the wavelength of the incident light. Afterwards, the threshold and hysteresis width of OB were adjusted by adjusting the position of MoS<sub>2</sub> embedded in the defect layer, the incident angle and the structural parameters of the defect layer. The scheme achieves controlled tuning of OB in the visible band band, and the structure of the scheme is easy to prepare. We believe that this research can provide a new tuning idea for the implementation of OB in optical fields such as all-optical switches and all-optical logic gates in the future.

## Acknowledgments

This work was supported by the Scientific Research Fund of Hunan Provincial Education Department (Grant No. 21B0048), Natural Science Foundation of Hunan Province (Grant Nos.2022JJ30394), the Changsha Natural Science Foundation (Grant Nos. kq2202236).

## References

- [1] Gibbs HM. Optical bistability controlling: light with light. Academic Press; 1985.
- [2] Notomi M, Shinya A, Mitsugi S, Kira G, and Tanabe T. Optical bistable switching action of si high-q photonic-crystal nanocavities. *Opt Express* 2005;3(7): 2678–87.
- [3] Nozaki K, Lacraz A, Shinya A, Matsuo S, Sato T, Takeda K, Kuramochi E, Noto M. All-optical switching for 10-Gb/s packet data by using an ultralowpower-optical bistability of photonic-crystal nanocavities. *Opt Express* 2015;23(23):30379–92.
- [4] Wen PY, Sanchez M, Gross M, and Esener S. Vertical-cavity optical AND gate. *Opt Commun* 2003;219(1):383–7.
- [5] Zhang WL, Jiang Y, Zhu YY, Wang F, Rao YJ. All-optical bistable logic control based on coupled Tamm plasmons. *Opt Lett* 2013;38(20):4092–5.
- [6] Li J, Liang S, Xiao S, He MD, L.H. Liu, Luo JH , Chen LQ. A sensitive biosensor based on optical bistability in a semiconductor quantum dot-DNA nanohybrid. *J Phys D Appl Phys* 2018;52(3):035401.
- [7] Tanabe T, Notomi M, Mitsugi S, Shinya A, Kuramochi E. Fast bistable all-optical switch and memory on a silicon photonic crystal on-chip. *Opt Lett* 2005;30(19): 2575–7.
- [8] Wu YC, Zhu Y, Liao XL, Meng JJ, He JJ. All-optical flip-flop operation based on bistability in V-cavity laser. *Opt Express* 2016;24(12):12507–14.
- [9] Shiri J, Khalilzadeh J, and Asadpour SH. Optical bistability in reflection of the laser pulse in a 1D photonic crystal doped with four-level InGa<sub>N</sub>/Ga<sub>N</sub> quantum

- dots. *Laser Phys.* 2021;31(3):036202.
- [10] Peng Y, Xu J, Dong H, Dai X, Jiang J, Qian S, Jiang L. Graphene-based low-threshold and tunable optical bistability in one-dimensional photonic crystal Fano resonance heterostructure at optical communication band. *Opt Express* 2020; 28(23):34948–59.
- [11] Yuan H, Jiang X, Huang F, Sun X. Ultralow threshold optical bistability in metal/randomly layered media structure. *Opt Lett* 2016;41(4):661–4.
- [12] Jiang LY, Guo J, Wu LM, Dai XY, Xiang YJ. Manipulating the optical bistability at terahertz frequency in the Fabry-Perot cavity with graphene. *Opt Express* 2015; 23(24):31181–91.
- [13] Kim M, Kim S, Kim S. Optical bistability based on hyperbolic metamaterials. *Opt Express* 2018;26(9):11620–32.
- [14] Wang ZP, Yu BL. Optical bistability and multistability in polaritonic materials doped with nanoparticles. *Laser Phys Lett* 2014;11(11):115903.
- [15] Mikhailov SA, Ziegler K. Nonlinear electromagnetic response of graphene: frequency multiplication and the self-consistent-field effects. *J Phys Condens Matter* 2008;20(38):384204.
- [16] Ooi KJA, Ang YS, Zhai Q, Tan DTH, Ang LK, Ong CK. Nonlinear Plasmonics of three-dimensional Dirac semimetal. *APL Photonics* 2019;4(3):034402.
- [17] Xiang YJ, Dai XY, Guo J, Wen SC, Tang D. Tunable optical bistability at the graphene-covered nonlinear interface. *Appl Phys Lett* 2014;104(5):051108.
- [18] Jiang LY, Tang J, Xu J, Zheng Z, Dong J, Guo J, Qian SY, Dai XY, Xiang YJ. Graphene tamm plasmon-induced low-threshold optical bistability at terahertz frequencies. *Opt Mater Express* 2019;9(1):139–50.
- [19] Long X, Bao Y, Yuan X, Zhang H, Dai XY, Li Z, Jiang LY, Xiang YJ. Low threshold optical bistability based on topological edge state in photonic crystal heterostructure with Dirac semimetal. *Opt Express* 2022;30(12):20847–58.
- [20] Wen X, Gong Z, Li D. Nonlinear optics of two-dimensional transition metal dichalcogenides. *InfoMat* 2019;1(3):317–37.
- [21] Bosshard C, Spreiter R, Zgonik M, Günter P. Kerr nonlinearity via cascaded optical rectification and the linear electro-optic effect. *Phys Rev Lett* 1995;

74(14):2816–19.

- [22] Balaei M, Karimzadeh R, Naseri T. Introducing a novel approach to linear and nonlinear electrical conductivity of MoS<sub>2</sub>. *Opt Mater Express* 2021;11(8): 2665–74.
- [23] Kavokin AV, Shelyk IA, Malpuech G. Lossless interface modes at the boundary between two periodic dielectric structures. *Phys Rev B* 2005;72(23):233102.
- [24] Brand S, Kalitchevski MA, Abram RA. Optical Tamm states above the bulk plasma frequency at a Bragg stack/metal interface. *Phys Rev B* 2009;79(8): 085416.
- [25] Sasin ME, Seisyan RP, Kalitchevski MA, Brand S, Abram RA, Chamberlain JM, Egorov AY, Vasil'ev AP, Mikhlin VS, Kavokin AV. Tamm plasmon polaritons: slow and spatially compact light. *Appl Phys Lett* 2008;92(25):251112.
- [26] Kalitchevski M, Iorsh I, Brand S, Abram RA, Chamberlain JM, Kavokin AV, Shelykh IA. Tamm plasmon-polaritons. Possible electromagnetic states at the interface of a metal and a dielectric Bragg mirror. *Phys Rev B* 2007;76(16): 165415.
- [27] Guo J, Sun Y, Zhang Y, Li H, Jiang H, Chen H. Experimental investigation of interface states in photonic crystal heterostructures. *Phys Rev E* 2008;78(2): 026607.
- [28] Chen Z, Han P, Leung CW, Wang Y, Hu M, Chen Y. Study of optical Tamm states based on the phase properties of one-dimensional photonic crystals. *Opt Express* 2012;20(19):21618–26.
- [29] Guo J, Jiang L, Jia Y, Dai X, Xiang Y, Fan D. Low threshold optical bistability in one-dimensional gratings based on graphene plasmonics. *Opt Express* 2017; 25(6):5972–81.
- [30] Hu T, Wang Y, Wu L, Zhang L, Shan Y, Lu J, Wang J, Luo S, Zhang Z, Liao L, Wu SW, Shen XC, Chen Zh. Strong coupling between Tamm plasmon polariton and two dimensional semiconductor excitons. *Appl Phys Lett* 2017;110(5): 051101.
- [31] Mukherjee B, Tseng F, Gunlycke D, Amara KK, Eda G, Simsek E. Complex electrical permittivity of the monolayer molybdenum disulfide (MoS<sub>2</sub>) in near

UV and visible. *Opt Mater Express* 2015;5(2):447–55.

[32] Shen CC, Hsu YT, Li LJ, Liu HL. Large dynamics and electronic structures of monolayer MoS<sub>2</sub> films grown by chemical vapor deposition. *Appl Phys Lett* 2013;6(12):125801.

[33] Zhang H, Long X, Yuan H, Dai X, Li Z, Jiang L, Xiang Y. Dirac Semimetals Tammplasmons-induced low-threshold optical bistability at terahertz frequencies. *Results in Physics* 2022;43:106054.